

pubs.acs.org/JACS Article

Presynthetic Redox Gated Metal-to-Insulator Transition and Photothermoelectric Properties in Nickel Tetrathiafulvalene-Tetrathiolate Coordination Polymers

Jiaze Xie,[§] Jia-Ahn Pan,[§] Baorui Cheng, Tengzhou Ma, Alexander S. Filatov, Shrayesh N. Patel, Jiwoong Park, Dmitri V. Talapin, and John S. Anderson*



Cite This: J. Am. Chem. Soc. 2022, 144, 19026–19037



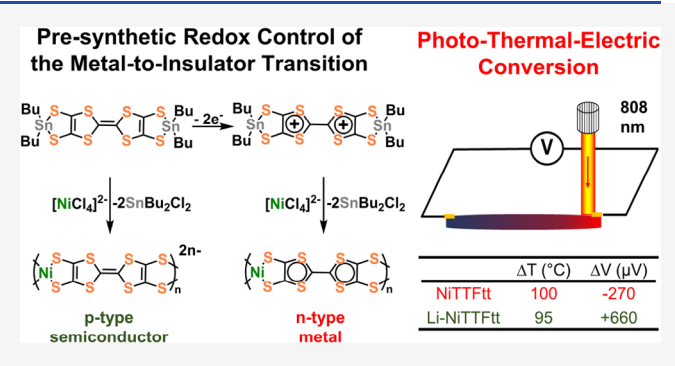
ACCESS I

III Metrics & More

Article Recommendations

Supporting Information

ABSTRACT: Photothermoelectric (PTE) materials are promising candidates for solar energy harvesting and photodetection applications, especially for near-infrared (NIR) wavelengths. Although the processability and tunability of organic materials are highly advantageous, examples of organic PTE materials are comparatively rare and their PTE performance is typically limited by poor photothermal (PT) conversion. Here, we report the use of redox-active Sn complexes of tetrathiafulvalene-tetrathiolate (TTFtt) as transmetalating agents for the synthesis of presynthetically redox tuned NiTTFtt materials. Unlike the neutral material NiTTFtt, which exhibits n-type glassy-metallic conductivity, the reduced materials $\text{Li}_{1.2}\text{Ni}_{0.4}[\text{NiTTFtt}]$ and [Li-



 $(THF)_{1.5}]_{1.2}Ni_{0.4}[NiTTFtt]$ (THF = tetrahydrofuran) display physical characteristics more consistent with p-type semiconductors. The broad spectral absorption and electrically conducting nature of these TTFtt-based materials enable highly efficient NIR-thermal conversion and good PTE performance. Furthermore, in contrast to conventional PTE composites, these NiTTFtt coordination polymers are notable as single-component PTE materials. The presynthetically tuned metal-to-insulator transition in these NiTTFtt systems directly modulates their PT and PTE properties.

INTRODUCTION

Photoelectric energy conversion, where light is converted into electricity, underpins solar energy capture and generation. The most general route is the direct capture of photons and conversion into an electrical potential through photovoltaic (PV) materials, such as emerging perovskite cells. Although the efficiency of perovskite PVs has dramatically increased to more than 25% from 3.8% in the last two decades, there are still fundamental challenges to the efficiency ceilings of this technology. For instance, it is reported that up to 40% of the thermodynamic loss in PVs occurs due to carrier thermal relaxation. Furthermore, the spectral windows of many PVs have a maximum onset of photogeneration around 800 nm, which means that nearly the entire near-infrared (NIR) spectrum is reflected or lost as waste heat.

In addition to direct PV capture of photons, an alternative route is photothermoelectric (PTE) conversion where light is converted into heat via a photothermal (PT) process, followed by a heat to voltage conversion in a thermoelectric (TE) process. The development of PTE devices or solar thermoelectric generators (STEGs) could feasibly increase the utilization of solar energy by both allowing the harvesting of waste heat as well as increasing the solar absorption window. However, the efficiency of STEGs is still limited by PT

efficiency and performance.^{6a} This motivates the development of new PTE materials.

Beyond energy capture, NIR-sensitive PTE materials also have utility in applications such as photodetectors⁷ and night vision cameras.⁸ A recent review has summarized the progress of photodetectors based on the PTE effect,⁹ suggesting that PTE devices can realize ultrabroadband photodetection without cooling units and external bias. Such characteristics are highly desirable in the military and civilian fields. For instance, the Mars Reconnaissance Orbiter launched by the National Aeronautics and Space Administration (NASA) in 2005 contained an uncooled PTE detector to monitor the climate of Mars.⁹

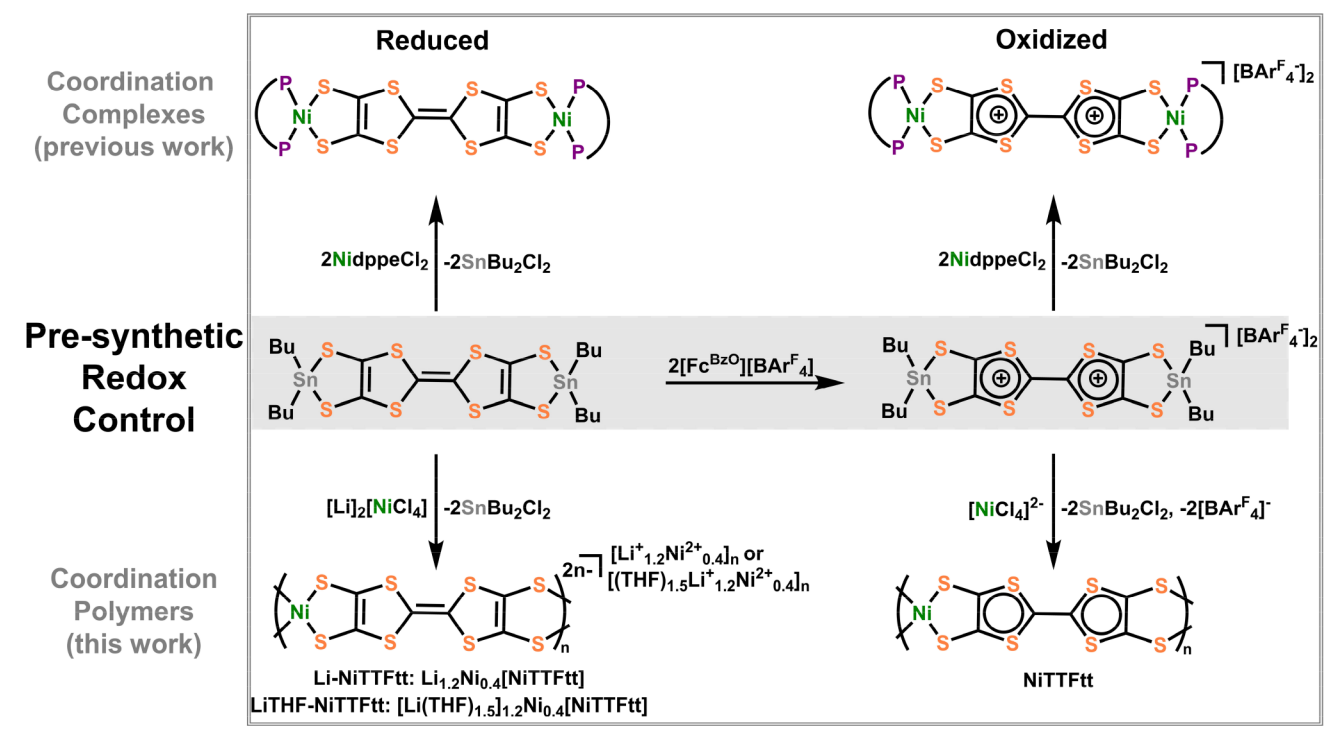
Although PTE effects have now been observed in a wide variety of materials, including 2D materials such as graphene and MoS₂, organic PTE materials are comparatively rare,

Received: July 25, 2022 Published: October 4, 2022





Scheme 1. Synthesis of Li-NiTTFtt, LiTHF-NiTTFtt, and NiTTFtt via Presynthetic Redox Control^a



^aThe synthetic strategy was developed in a previous molecular study (top, ref 23).

particularly for NIR applications. Conducting organic polymers are an important branch of TE materials as they are light and flexible and exhibit intrinsically low thermal conductivity. New TE organic materials with prominent PT effects are promising candidates for wearable PTE devices, as reported for NIR-sensitive poly(3,4-ethylenedioxyselenophene) (PEDOS) derivatives which generate an output voltage of 900 μ V in 3 s under 808 nm laser irradiation (2.33 W/cm²). This work demonstrates the potential of organic materials in PTE applications, but this field is still under-explored. Indeed, aside from another single report of Cu-ethylenetetrathiolate (ett) polymers from 2015, there are no other examples of organic PTE materials.

Tetrathiafulvalene (TTF)-based charge transfer salts and metal—organic frameworks (MOFs) have recently been reported to exhibit excellent NIR PT conversions. Hone example is even able to heat up to 250 °C in 25 s under 0.4 Wcm⁻² irradiation at 808 nm. Had This rapid and efficient performance suggests that TTF-based materials exhibit exceptional PT properties, but the conductivity required for PTE applications is still a limitation in this area.

Despite this issue, there have been enormous strides in realizing conductive coordination polymers (CPs) over the past decade. Conducting CPs or MOFs¹⁵ have shown promising applications in superconductors,¹⁶ energy storage,¹⁷ TEs,¹⁸ and other applications.¹⁹ Among many conductive motifs, dithiolene-based frameworks in particular exhibit significant delocalization and high conductivity due to better energy match between sulfur atoms and metal centers.²⁰ The poor thermal conduction of organic components also makes dithiolene-based CPs potential candidates for TEs. For example, in 2016, a ZT value of 0.30 (3) was reported for Ni-ett chains.^{18c} In addition to thermal and electrical conductivity, square-planar bis(dithiolene) complexes are also

commonly characterized with strong NIR absorptions as well as PT conversion properties. Some materials have been developed for PT therapy and photo-controlled drug delivery. ²¹

Our laboratory has been interested in TTF-based materials, particularly those composed of tetrathiafulvalene-tetrathiolate units (TTFtt). We recently reported that neutral NiTTFtt has remarkably high conductivity and glassy-metallic character while being stable to heat, air, and acid/base.²² Given the exemplary PT properties of TTF units and metal-dithiolenes in other reports, we hypothesized that these materials could be good candidates for PTE applications. Furthermore, we rationalized that modulating the redox state of these materials via presynthetic redox changes on the TTFtt linker precursors might enable tuning of their PT or TE properties and hence would reveal a new strategy for designing PTE properties in new materials. Here, we demonstrate that this strategy of presynthetic redox manipulation,²³ using either neutral TTFtt- $(SnBu_2)_2$ or dicationic $[TTFtt(SnBu_2)_2][BAr_4^F]_2$ $(BAr_4^F)_2$ tetrakis(3,5-bis(trifluoromethyl)phenyl)borate; Bu = n-Butyl) as the transmetalating precursor, enables control over the redox state of NiTTFtt CPs. In addition to the previously reported neutral NiTTFtt material (NiTTFtt), using TTFtt-(SnBu₂)₂ leads to reduced NiTTFtt²⁻ chains, with Li⁺ and $Li(THF)_x^+$ (THF = tetrahydrofuran) as counter ions, in the materials Li_{1.2}Ni_{0.4}[NiTTFtt] (Li-NiTTFtt) and [Li- $(THF)_{1.5}]_{1.2}Ni_{0.4}[NiTTFtt]$ (LiTHF-NiTTFtt), respectively. Interestingly, unlike n-type metallic NiTTFtt, physical characterization suggests that these reduced polymers are typical p-type semiconductors. The broad spectral absorption and electrically conducting nature of these TTFtt-based materials enable highly efficient NIR-thermal conversion and good PTE performance. Furthermore, tuning of the PTE performance can be achieved by changing the redox states of

the TTFtt ligands in these materials. Unlike conventional STEGs made of several different materials combined in a composite, the materials presented here are single-component PTE candidates. Such single-component materials are desirable for ease of device fabrication and durability of performance. The NiTTFtt systems reported here represent the best singlecomponent organic PTE materials for both p-type and n-type applications. The tunable PT, TE, conductivity, and carrier properties of this system demonstrate that using synthetic strategies to rationally change the redox states of CPs is a powerful route for generating new PTE candidates and other functional materials. Since LiTHF-NiTTFtt contains the same NiTTFtt²⁻ chains as Li-NiTTFtt but has solvated-lithium counter ions, only Li-NiTFtt and NiTTFtt have been investigated for PTE and PT properties to avoid convolutions from desolvation under heating.

RESULTS AND DISCUSSION

Synthesis and Redox Control. NiTTFtt is synthesized by transmetallation of $[TTFtt(SnBu_2)_2][BAr^F_4]_2$ with excess $[TEA]_2[NiCl_4]$ (TEA = tetraethylammonium). To investigate the formation of alternative redox isomers of this material, the neutral linker precursor $TTFtt(SnBu_2)_2$ was reacted with in situ formed $Li_2[NiCl_4]$ in THF resulting in new CPs with anionic $NiTTFtt^2$ chains (Scheme 1). The counter ions for these chains depend on the workup of the material and are either $Li(THF)_x^+$ in the as-synthesized material LiTHF-NiTTFtt or Li^+ in the more-thoroughly dried material LiNiTTFtt. The different redox states of the TTF linkers in these materials are immediately apparent in their air stability. Unlike NiTTFtt, Li-NiTTFtt and LiTHF-NiTTFtt are extremely sensitive to air or chemical oxidants. As such, the characterization of these materials was carried out under anaerobic conditions.

We initially turned to characterizing the composition and formulae of these materials by a suite of techniques including X-ray fluorescence (XRF) spectroscopy, inductively coupled plasma-optical emission spectroscopy/mass spectrometry (ICP-OES/MS), and X-ray photoelectron spectroscopy (XPS) (see the Supporting Information). All analyses suggest a Ni/S ratio of 1:5.7 (1.4:8) and a Li/Ni ratio of 0.9:1 (1.2:1.4) in LiTHF-NiTTFtt and Li-NiTTFtt, which gives a formula of Li_{1.2}Ni_{1.4}C₆S₈ with only trace Sn (0.03:1 Sn/Ni) which we assign to chain ends (Table S1). This empirical formula suggests that Ni ions are not only incorporated into the backbone of the material but also serve as counter cations, as has been observed in other Ni-bisdithiolene polymers. 186 Multiple chemical environments for Ni are also supported by the fact that Ni-K edge X-ray absorption near edge structure (XANES) spectra of Li-NiTTFtt and LiTHF-NiTTFtt (Figure 1) are different in shape/structure from that of NiTTFtt, albeit with identical K-edge positions which suggest similar Ni(II) oxidation states. In the Ni K-edge XANES spectrum of NiTTFtt, the peak localized at 8338.6 (4) eV corresponds to a 1s-4p_z transition with an additional "shakedown" transition. The intensity of this feature is dependent on the geometry at Ni, with D_{4h} symmetric centers giving rise to this intense signal.²⁴ Thus, the XANES spectra for Li-NiTTFtt and LiTHF-NiTTFtt are a combination of the D_{4h} Ni centers in the chains and signals from any Ni counter cations. Fits of the extended X-ray absorption fine structure (EXAFS) of Li-NiTTFtt with a simple Ni bisdithiolene model suggest Ni-S bond lengths of 2.161 (6) Å, which are very similar to the Ni-

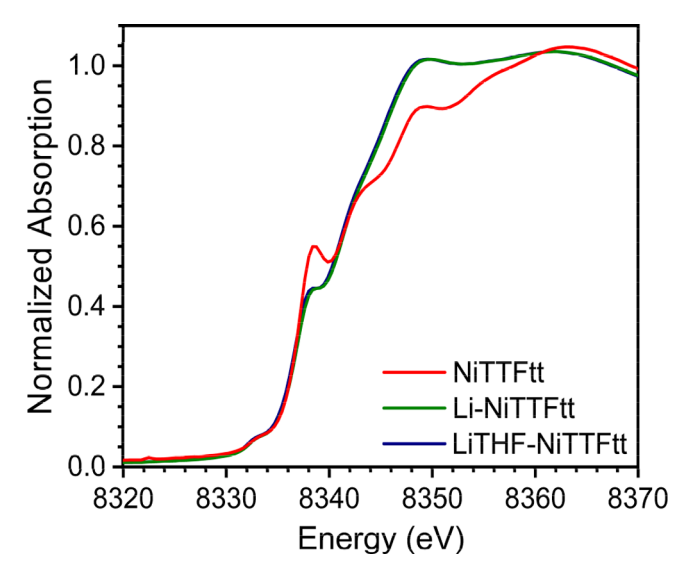


Figure 1. Ni K-edge XANES spectra of LiTHF-NiTTFtt (blue), Li-NiTTFtt (green), and NiTTFtt (red).

S bonds in NiTTFtt of 2.177 (9) Å (Table S3). The similarity of these distances supports similar structures and Ni(II) oxidation states for both materials indicating that the redox differences between these two materials are TTFtt-based. However, we note that the presence of the additional Ni(II) counter cations, whose positions are unclear and have not been modeled, is a convoluting factor in interpreting structural parameters from X-ray absorption spectroscopy (XAS). Nevertheless, accounting for Ni(II) counter cations verifies the presence of reduced chains with an overall 2— charge, indicating that a formally neutral TTF core is maintained in the final products. Combustion analysis (Table S2) further confirms the formula assignments of [Li_{1.2}Ni_{0.4}]NiTTFtt for LiTHF-NiTTFtt

In addition to the composition analysis, we also attempted to interrogate redox differences spectroscopically. While XPS characterization of the S 2p peaks to assign redox states is ambiguous due to multiple sulfur chemical sites (Figure S2), we did observe a Raman band for NiTTFtt at around 1100 ${\rm cm}^{-1}$, corresponding to $v_{\rm CS}$ modes (Figure 2, red). This feature shifts to 950 cm⁻¹ in the case of the reduced congener Li-NiTTFtt (Figure 2, green). Similar shifts to lower energy have been observed in $TTF[Ni(dmit)_2]_2$ (dmit = 1,3-dithiole-2thione-4,5-dithiolate) systems with the general interpretation that higher frequencies indicate more positive charge character on the organic fragment.²⁵ This supports the conclusion from XAS of ligand-based redox changes. While the Raman spectrum of LiTHF-NiTTFtt is convoluted by overlapping THF vibrational modes, an absorption at 950 cm⁻¹ is apparent in infrared spectra of both Li-NiTTFtt and LiTHF-NiTTFtt (Figure 4E) but absent in that of NiTTFtt, which supports similar oxidation states in the two reduced materials.

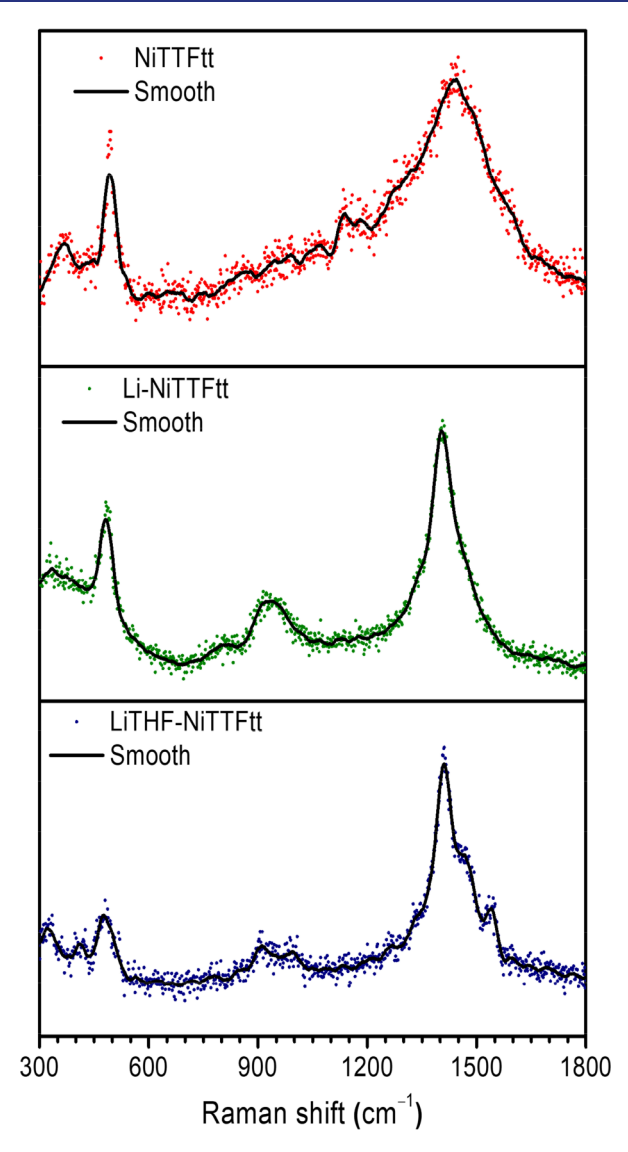


Figure 2. Raman spectra of LiTHF-NiTTFtt (blue), Li-NiTTFtt (green), and NiTTFtt (red).

the possibility that these features arise from the dithiolene moieties. ²³ Regardless, all observed redox potentials are shifted cathodically compared to the molecular analogue (TTF/TTF⁻⁺/TTF²⁺, -0.58 and -0.11 V; Ni^{II}/Ni^{III}, 0.79 V). The exact reason for this shift is not immediately apparent but may be due to differences in packing and negative charge delocalization. Regardless, these negative potentials provide a possible rationale for the empirical formulas of early reports of NiTTFtt materials which indicate partial oxidation. ²⁶ Indeed, we noticed that in our hands the use of typically redox-neutral solvents such as methanol (as widely used in the literature) in Li-NiTTFtt syntheses resulted in oxidized materials. This observation underscores the importance of using rigorously anaerobic and anhydrous conditions to access different redox congeners of dithiolene-based materials in a reliable manner.

Redox Induced Crossing of the Metal-to-Insulator Transition. Once we had established the overall composition of these materials, we then turned to examine their electrical properties. Compared to NiTTFtt, which is highly conductive $(4.7 (3) \times 10^2 \text{ S/cm}, \text{ four-probe, room-temperature pressed pellets})$, the room-temperature conductivities of Li-NiTTFtt (10 (1) S/cm, four-probe; 1.7 (8) S/cm, two-probe) and

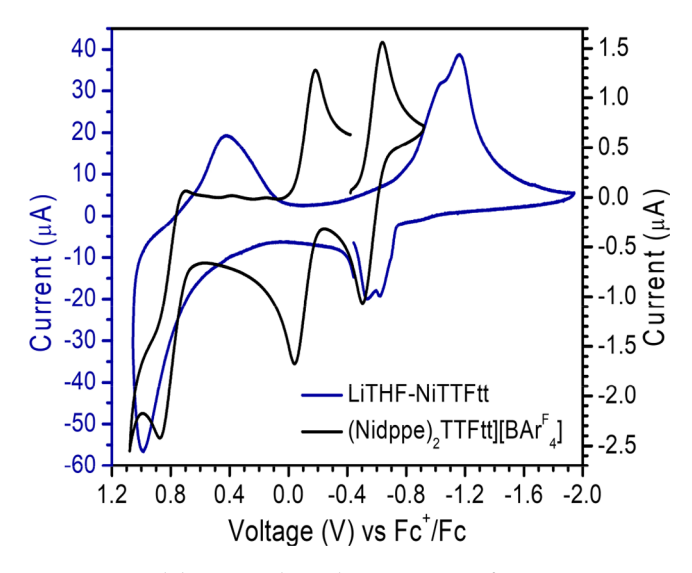


Figure 3. Solid-state cyclic voltammograms of **LiTHF-NiTTFtt**. Conditions: 0.1 M LiPF $_6$ /MeCN at a 10 mV/s scan rate. The CV plot of molecular [(Nidppe) $_2$ TTFtt][BAr $_4$] is replotted from previously published data. ²³

LiTHF-NiTTFtt (1.2 (9) \times 10⁻⁵ S/cm, two-probe) are much lower. Additionally, the Seebeck coefficients of Li-NiTTFtt and LiTHF-NiTTFtt are positive at +10.0 (6) and +31.5 (4) μ V/K, respectively, which is notably different than a value of -3.6 (1) μ V/K found in NiTTFtt (Figure 4A). The sign of the Seebeck coefficients and the measured conductivity suggest that the reduced NiTTFtt²⁻ materials are p-type semiconductors. The differing metal/semiconductor character of these redox congeners is also supported by ultraviolet photoelectron spectroscopy (UPS) analysis where the work function cut off at about 0.5 eV in Li-NiTTFtt and LiTHF-NiTTFtt is notably distinct from that in NiTTFtt (Figure 4B).

To further study the charge transport mechanism of these materials, we carried out variable-temperature resistance measurements on Li-NiTTFtt and LiTHF-NiTTFtt. As shown in Figure 4C, the resistances of both Li-NiTTFtt and LiTHF-NiTTFtt materials increase exponentially as the temperature decreases, in contrast to the resistance curve of NiTTFtt which is almost flat. Arrhenius fits above 200 K provide activation energies of Li-NiTTFtt and LiTHF-NiTTFtt of ~0.18 and ~0.23 eV, respectively. The temperature-dependent conductivity behaviors deviate from the Arrhenius law at low temperatures, especially for Li-NiTTFtt (Figure S13). Therefore, 3D Mott variable-range hopping (3D VRH) models were applied as shown in Figure 4D. We recently reported a characteristic temperature, T_0 , value extracted from this 3D VRH analysis on a NiTTFtt pellet which is extremely small, 13 K. Such a value is consistent with a metallic glass $(T_0 1-10^4 \text{ K})^{27}$ but not with a semiconductor. In contrast, the obtained T_0 values for Li-NiTTFtt and LiTHF-NiTTFtt are 5.1×10^6 and 1.1×10^9 K, respectively, which are typical for amorphous semiconductors.²⁷ The larger T_0 value of LiTHF-NiTTFtt implies a lower density of states at the Fermi level as compared to Li-NiTTFtt. Taken together with the larger Seebeck coefficient of LiTHF-NiTTFtt, these results may suggest that larger counter ions between chains increase hopping barriers and lower carrier concentrations in these materials.

Semiconducting molecular materials commonly exhibit longwavelength absorptions in their IR spectra due to the small 10

10

50

100

150

Temperature (K)

200

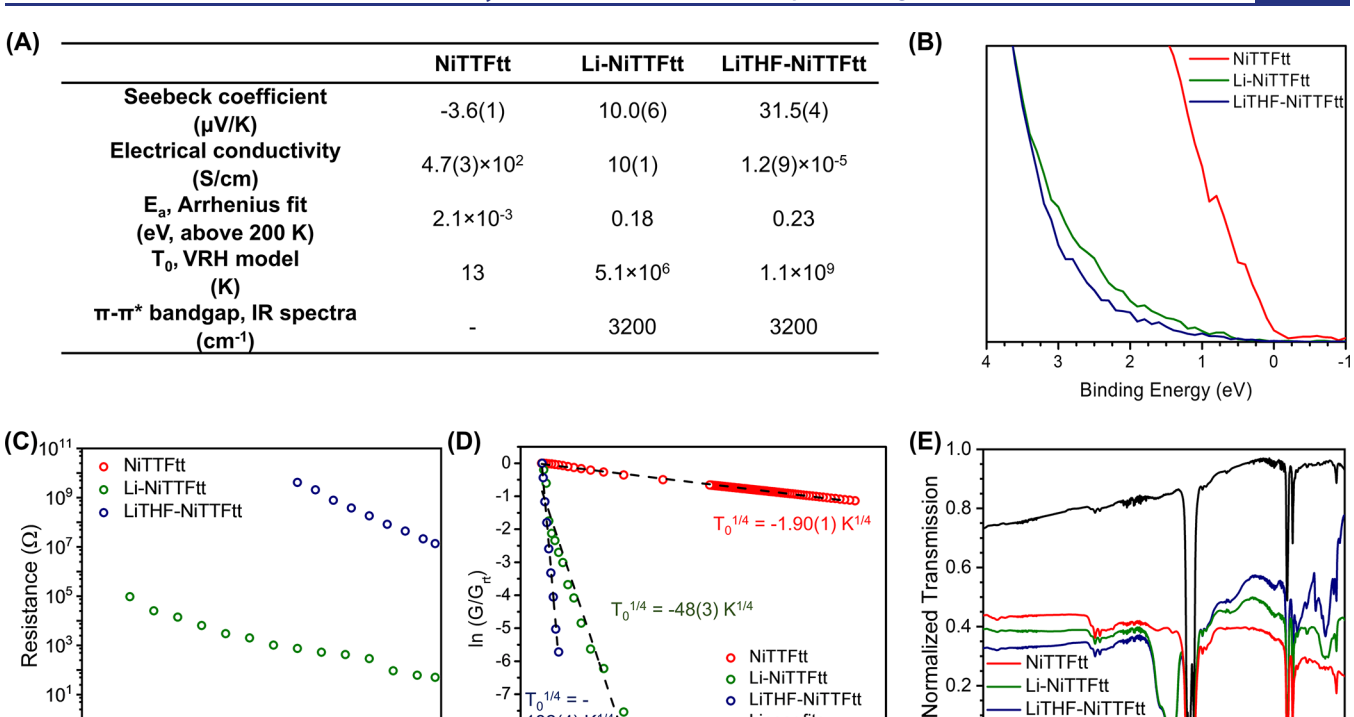


Figure 4. Physical characterization supporting a metal-to-insulator transition via redox control. (A) Summary of each species' physical properties. (B) Ultraviolet photoelectron spectra. (C) Plots of variable-temperature resistance. (D) 3D Mott variable-range hopping models and linear fits. (E) IR transmittance spectra (baselined) as Nujol mulls. Blue: LiTHF-NiTTFtt; green: Li-NiTTFtt; red: NiTTFtt.

 $T^{-1/4} (K^{-1/4})$

0.3 0.4 0.5 0.6 0.7 0.8

Li-NiTTFtt

Linear fits

LiTHF-NiTTFtt

HOMO–LUMO gaps of delocalized π -systems. ²⁸ In the case of these NiTTFtt²⁻ chains, we also found a strong and broad absorption around 3200 cm⁻¹ in the IR spectra of both Li-NiTTFtt and LiTHF-NiTTFtt (Figure 4E). The energy of this feature indicates a $\pi-\pi^*$ bandgap of about 0.4 eV. Notably, this absorption band is absent in NiTTFtt which also supports a metallic transition upon oxidation. Similar trends have been observed in TTF-based organic metals. 28,29 Hence, this phenomenon is a further support of a metal-to-insulator transition upon reduction of the NiTTFtt chains.

250

300

In summary, all physical characterization supports that these reduced polymers are p-type semiconductors with bandgaps of ~0.2 to 0.4 eV, in contrast to the oxidized material NiTTFtt which is metallic. Furthermore, we observe that the large counterion seemingly plays an important role in hopping transport between neighboring chains, as LiTHF-NiTTFtt exhibits significantly lower conductivity.

NIR Photothermal Conversion. Despite different charge transport mechanisms, diffuse reflectance spectra demonstrate that all three materials have broad absorptions over the visible and NIR regions (Figure 5). These broad absorptions suggest that these materials may effectively capture light, and particularly low-energy light, to convert it into thermal energy.

Since LiTHF-NiTTFtt becomes desolvated with sufficient heating, only Li-NiTTFtt and NiTTFtt were tested for NIR PT behavior. Before testing PT conversion, the thermal stabilities of Li-NiTTFtt and NiTTFtt were examined by thermogravimetric analysis (TGA, Figure S14) and differential scanning calorimetry (DSC, Figure S15). Both materials are stable up to at least 150 °C under appropriate testing conditions (Li-NiTTFtt under N₂ gas and NiTTFtt in air). Encouraged by this stability, we recorded the temperature of

pressed pellets under 808 nm laser irradiation using an IR thermal camera. As shown in Figure 6A, NiTTFtt shows a linear temperature increase to values as high as 120 °C in 20 s when scanning the light power density from 0.50 to 2.0 W/ cm². Similar behavior is observed with Li-NiTTFtt pellets with a maximum of 118 °C in 30 s at a much lower power density of 0.40 W/cm² (Figure 6D). Linear fits reveal a temperature rise of 4.4 and 23 K per 0.1 W/cm² radiation for NiTTFtt and Li-NiTTFtt, respectively (Figure 6C). The performances of these materials, particularly with regard to the magnitude and speed of their PT response, are excellent: the performance of Li-NiTTFtt is among the best reported for TTF-based materials.¹⁴ Samples maintained their performance even after exposure to 10 laser on/off cycles (1.5 Wcm⁻² for NiTTFtt and 0.30 Wcm⁻² for Li-NiTTFtt, Figure 6B,E).

0.2

0.0

6000

Li-NiTTFtt

blank

5000

LiTHF-NiTTF#

4000

3000

Wavenumber (cm⁻¹)

2000

1000

To assess the efficiency of the light-to-heat conversion, the PT efficiency, η_{PT} , was determined with a modified Roper's model (via a cooling process), 30 from the following equation:

$$\eta_{\text{PT}} = \frac{hS\Delta T_{\text{max}}}{I(1 - 10^{-A_{\text{S0S}}})} = \frac{\sum_{i} m_{i} C_{\text{p}_{i}} \Delta T_{\text{max}}}{\tau I(1 - 10^{-A_{\text{S0S}}})}$$

$$\geq \frac{mC_{\text{p}} \Delta T_{\text{max}}}{\tau I(1 - 10^{-A_{\text{S0S}}})}$$

where I is the laser power; A_{808} is the absorbance of the materials at a wavelength of 808 nm; h is the heat transfer coefficient; S is the surface area of the system; m_i and C_{pi} are the mass and heat capacity of the system components, respectively; au is the cooling time coefficient; $\Delta T_{
m max}$ is the temperature difference between the maximum and the ambient temperature.

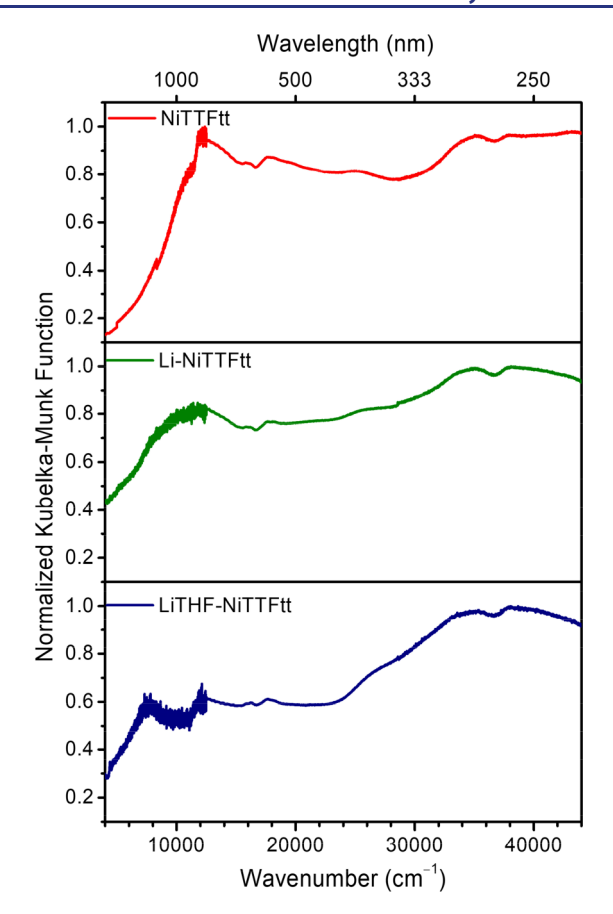


Figure 5. UV—vis—NIR diffuse reflectance spectra of LiTHF-NiTTFtt (blue), Li-NiTTFtt (green), and NiTTFtt (red) using KCl as a nonabsorbing matrix.

Since the samples were laid on a white thermally insulated foam, which displayed no detectable temperature change during the experiments, we assume that the heat was only maintained in the pellet at thermal equilibrium. We determined the materials' specific heats by DSC (Figures S16 and S17), revealing values of 0.87 (1) $Jg^{-1}K^{-1}$ for NiTTFtt and 0.86 (4) $Jg^{-1}K^{-1}$ for Li-NiTTFtt. The value of τ was determined by fitting the decay behavior of the temperature after the laser was turned off (Figure S19) which provided values of 7.2 (1) and 8.2 (2) s for NiTTFtt and Li-NiTTFtt, respectively. The absorbance of NiTTFtt at 808 nm was determined from its specular reflectance spectrum (6% reflectance vs Al). Due to air sensitivity, we were unable to collect the specular reflectance spectrum of Li-NiTTFtt. However, as both NiTTFtt and Li-NiTTFtt have strong absorptions in the NIR region, the A_{808} of Li-NiTTFtt here was assumed to be the same as that of NiTTFtt. With all these parameters, the PT efficiencies of NiTTFtt and Li-NiTTFtt are estimated to be 71 and 94% (Figure 6F), respectively, which are higher than those of the best reported organic PT materials (71%) and even higher than those of many inorganic materials such as Au nanoparticles and quantum dots.³

The similar cooling coefficients of NiTTFtt and Li-NiTTFtt suggest that their different PT performance arises from differing efficiency in PT capture. While a detailed understanding of the PT mechanism in these two materials is not yet clear, we propose that NiTTFtt, which is best described as a metal, and Li-NiTTFtt, which is a semiconductor, may have very different PT mechanisms which could explain their

different PT capture efficacies. However, the above results demonstrate that both NiTTFtt and Li-NiTTFtt possess (1) broad absorption spectra stretching into the NIR; (2) a high temperature rise per unit power; (3) excellent stability and reproducibility; and (4) remarkable PT conversion efficiency. These features, combined with the electrical conductivity of these material, are promising for PTE conversion, and thus, we then investigated these materials in that context.

NIR-Seebeck Voltage. The PTE performance was studied by measuring the Seebeck voltage of pressed pellets under different NIR irradiation powers using a homemade setup (Figures S20 and S21). Two diametrical ends of a circular pellet were contacted with gold or silver paste, while one (hot) end was irradiated with a laser (Figure 7A). The temperatures of the cold and hot ends were monitored with an IR thermal camera. As shown in Figure 7D, the temperature rise and the generated voltage were linearly dependent on the NIR laser power for both Li-NiTTFtt and NiTTFtt, while the sign of the voltage was reversed as expected due to the different charge carriers present in the two materials. It is noteworthy that the PTE responses for both materials, which are about 12 s for Li-NiTTFtt and 1.5 s for NiTTFtt (Figure 7B,E), reach equilibrium much faster than their PT effects. The substrate represents a significant cooling pathway which plays an important role in the PTE responsivity and response time. The response time can be dramatically improved with a moderate sacrifice in responsivity by replacing the substrate with other materials with low thermal conductivity, a strategy which has been widely adopted in thin film-based PTE detectors. 9,32 Therefore, the response time of both Li-NiTTFtt and NiTTFtt can be further improved as needed via simple modifications of the sample holder. Finally, we note that the calculated values of the Seebeck coefficients from PTE experiments (Figure S22), $\sim -2.9 \ \mu V K^{-1}$ for NiTTFtt and 9.1 μ VK⁻¹ for Li-NiTTFtt, are consistent with the values measured within a Peltier setup at room temperature (-3.6 (1)) $\mu V K^{-1}$ and 10.0(6) $\mu V K^{-1}$, respectively).

Optimized polyselenophene films exhibited a temperature rise of $\sim\!15~\rm Kcm^2/W$ under 808 nm laser irradiation with $\eta_{\rm PT}=42.5\%$. Correspondingly, the previously reported Seebeck voltage is about 420 $\mu\rm Vcm^2/W$. 12 Under the same conditions, the produced voltage of Li-NiTTFtt is 1700 $\mu\rm Vcm^2/W$. Previously reported Cu-ett materials have PTE voltages that are also significantly smaller at $\sim\!360~\mu\rm Vcm^2/W$. 13 While this work was the first example of a single-component organic PTE material with a record PT efficiency for NIR light, the PT and PTE performances of the p-type Li-NiTTFtt material substantially exceed these pioneering organic materials. On the other hand, NiTTFtt is the first n-type organic PTE material to be reported to our knowledge.

Importantly, both **NiTTFtt** and **Li-NiTTFtt** pellets show reproducible PTE effects; the light-driven voltage was stable over multiple cycles of NIR switching (Figure 7C,F). Considering that the temperature change here is over 60 °C, in contrast to a much smaller 9 °C change in PEDOS films, ¹² this stability is notable, particularly for **NiTTFtt** which exhibited this stability in air.

We note that the source of the PTE efficiency in these NiTTFtt materials is different from conventional PTE materials that typically possess high Seebeck coefficients but low PT conversion. The TE properties of both NiTTFtt and Li-NiTTFtt are comparatively poor, and the PTE properties primarily arise from excellent PT conversion. Such effective PT

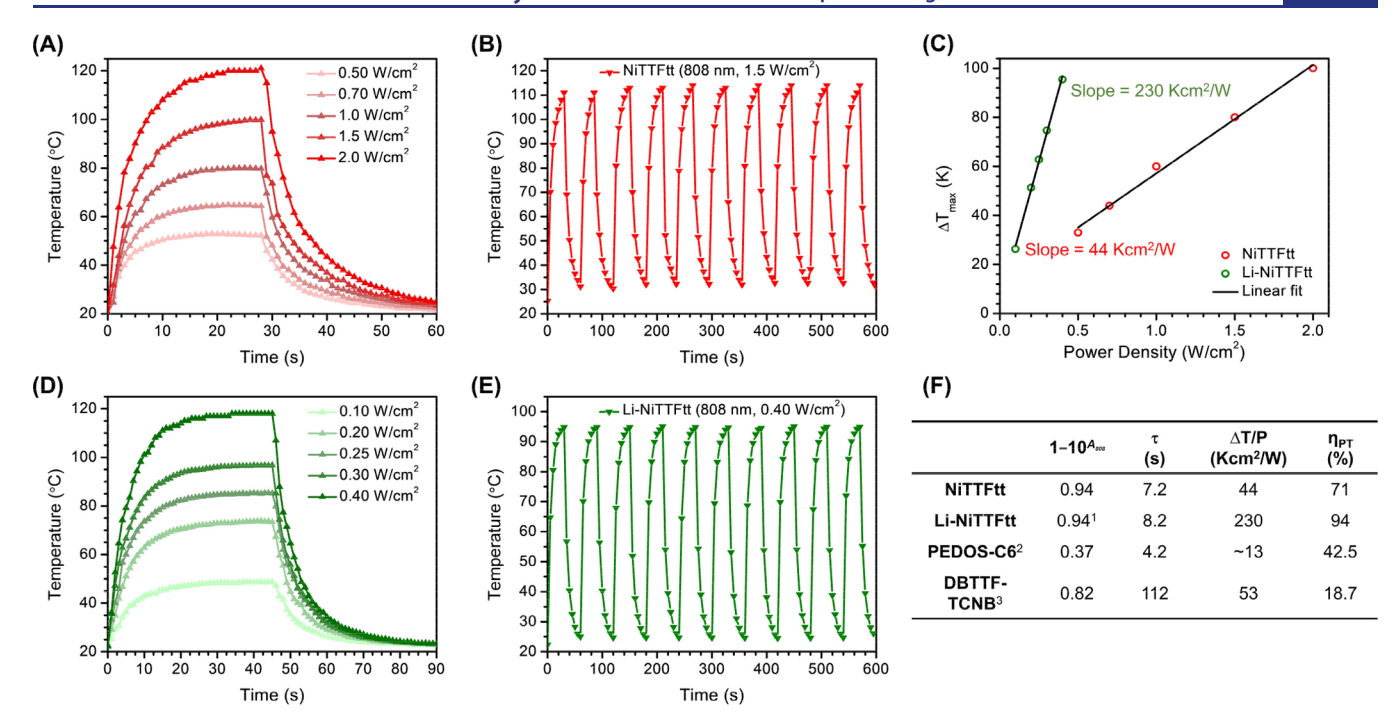


Figure 6. Photothermal conversion of NiTTFtt (red) and Li-NiTTFtt (green). (A) Temperature with different NIR laser power densities (808 nm) of a NiTTFtt pellet. (B) Reproducibility tests on a NiTTFtt pellet at 1.5 Wcm⁻² (ten heating—cooling cycles). (C) Linear relationships between temperature and irradiation power densities. (D) Temperature with different NIR laser power densities (808 nm) of a Li-NiTTFtt pellet. (E) Reproducibility tests on a Li-NiTTFtt pellet at 0.30 Wcm⁻² (ten heating—cooling cycles). (F) Comparison of PT parameters between NiTTFtt materials and other reported organic PT materials. P is the power density of 808 nm irradiation. Note: experiments on Li-NiTTFtt were performed in a N₂-filled glovebox with the same setup as that of NiTTFtt. ¹The absorption of Li-NiTTFtt is assumed to be identical to that of NiTTFtt for efficiency estimates due to their similar NIR absorption; ²ref 12; ³ref 14a.

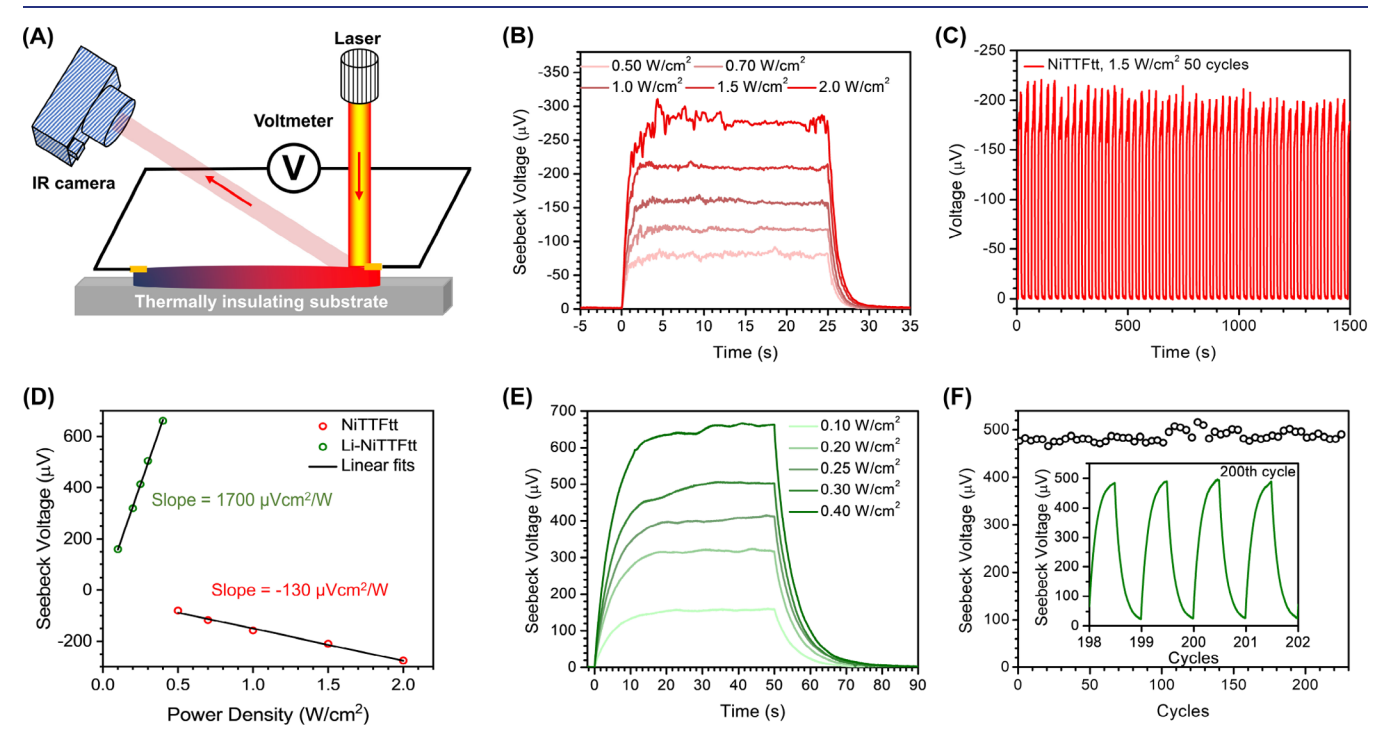


Figure 7. NIR-Seebeck voltage production from pellets of NiTTFtt (red) and Li-NiTTFtt (green). (A) Diagram of the photothermal voltage measurements. (B) Seebeck voltage generated from a NiTTFtt pellet with various NIR laser intensities. (C) Cycling tests on NiTTFtt with a NIR laser intensity of 1.5 Wcm⁻² at a switching time of 15 s. (D) Linear relationships between Seebeck voltages and irradiation power densities. (E) Seebeck voltage generated from a Li-NiTTFtt pellet with various NIR laser intensities. (F) Cycling tests on Li-NiTTFtt with a NIR laser intensity of 0.30 Wcm⁻² at a switching time of 20 s. Note: experiments on Li-NiTTFtt were performed under the same conditions as the above PT experiments.

conversion leads to a significant temperature difference which is needed to optimize TE efficiency in STEGs. 6a As such, preserving this excellent PT conversion while improving the Seebeck coefficients of these materials is a promising strategy for improved PTE conversion. Indeed, we note that the NiTTFtt system itself provides the opportunity to chemically tune PTE properties. We have thus far explored the behaviors of NiTTFtt and Li-NiTTFtt, which are the two extreme oxidation states of the NiTTFtt system. However, presynthetic redox control of the TTFtt-tin transmetalation precursors also allows for programming intermediate oxidation states. This strategy should enable tuning of the Seebeck coefficient and ZT figures similarly to how these parameters can be optimized via doping of conducting polymers.³³ Second, the counter ion size and identity is another dimension for chemical modulation, as suggested by the significantly different conductivities and Seebeck coefficients of Li-NiTTFtt and LiTHF-NiTTFtt. Larger counter ions may significantly reduce the carrier concentrations, which in turn would magnify the Seebeck coefficient and voltage. We hypothesize that the TE performance of these materials can be enhanced by selecting counter ions with suitable sizes, such as tetralkylammoniums. Finally, installation of different transition metals in the chain skeleton is another approach to tune properties. The electron density on the metal will affect the chain's band-filling, the identity of the charge carriers, and their concentration. In addition to chemical modifications, the different charge carriers in NiTTFtt and Li-NiTTFtt suggest that the fabrication of conventional p-n type TE devices using NiTTFtt and Li-NiTTFtt should provide an attractive route to develop highperformance PTE systems. Furthermore, while the isolated products LiTHF-NiTTFtt, Li-NiTTFtt, and NiTTFtt are completely insoluble black powders, we do note that synthetic mixtures of these materials display enhanced solubility over short times (<1 day), suggesting the possibility of solution deposition and processing. Although this work is focused on the intrinsic physical properties of NiTTFtt materials and their single-component PTE performance, matching NiTTFtt with other suitable components in practical devices, such as recent reports of STEG composites, 34 is a promising direction. Overall, the modular properties of this metal-organic material offer a great deal of promise for tunable properties in PT, TE, and PTE applications.

CONCLUSIONS

In this work, we demonstrate that presynthetic redox control enables us to isolate both reduced and oxidized NiTTFtt chains. Reduction of the TTFtt linkers results in the n-type metallic NiTTFtt polymer becoming p-type semiconductors. Comprehensive physical characterization of optical, thermal, and electrical properties demonstrates that these conducting NiTTFtt polymers exhibit efficient and high-performance PT conversion for NIR light. Furthermore, the heat generated from this conversion also shows promise in PTE applications, particularly for single-component organic materials. Considering the broad UV to NIR optical absorption, as well as fast and intense PTE responses, these materials also show potential in broadband PTE optical detector applications.

EXPERIMENTAL SECTION

General Methods. Unless otherwise noted, all synthetic manipulations were performed in a N2-filled MBraun UNILab glovebox. Dichloromethane was initially dried and sparged with Ar

on a solvent purification system from Pure Process Technologies and stored over 4 Å molecular sieves. Methanol (MeOH) was dried with NaOH and distilled before being transferred into the glovebox. The dried MeOH was then passed through activated alumina and stored over 4 Å molecular sieves in the glovebox. Tetrahydrofuran (THF) was stirred with liquid NaK alloy, filtered through activated alumina, and stored over 4 Å molecular sieves. TTFtt(SnBu₂)₂ (TTFtt = tetrathiafulvalene-2,3,6,7-tetrathiolate; Bu = n-butyl), FcBzOBArF $(Fc^{BzO} = benzoyl ferrocenium; ([BAr^{F_4}] = tetrakis(3,5-bis-$ (trifluoromethyl)phenyl)borate), Ni(DME)Cl₂ (DME = 1,2-dimethyloxyethane), and NiTTFtt were synthesized following previously reported procedures. 22,23,35 Combustion elemental analyses (C, H, and N) were performed by Midwest Microlabs. Except for PT- and PTE-related experiments, the data involved with NiTTFtt were all reproduced from ref 22.

LiTHF-/Li-NiTTFtt. TTFtt(SnBu₂)₂ (0.500 mmol, 400 mg) in 6 mL of THF was added into a 12 mL THF solution of Ni(DME)Cl, (0.500 mmol, 110 mg) and LiCl (2.50 mmol, 105 mg) with vigorous stirring for 40 min. The immediate precipitate was isolated via centrifugation and washed with THF (5 × 12 mL). After being dried under vacuum for 30 min until visibly dry, the dark purple powders were collected as LiTHF-NiTTFtt. To keep batch-to-batch consistency, the evacuation time was kept to exactly 30 min and the product LiTHF-NiTTFtt was stored in a -35 °C freezer to avoid solvent loss over time. Then, 131 mg of Li-NiTTFtt was isolated as a black powder (85%) after further evacuation of LiTHF-NiTTFtt at 100 °C overnight. Detailed characterization and composition data are provided in the main text as well as below.

Pressed pellets were prepared at 800 MPa in a glovebox by using a hydraulic pellet press (TMAX-15T) and dies with different sizes (7 and 8 mm round dies and 6 mm square dies). Prior to pressing, powders were ground to particle sizes below 20 µm. During pressing, the pressure was maintained for 20 min after stabilizing at 800 MPa. The thickness of the pressed pellets is around 100-300 μ m.

Inductively Coupled Plasma-Mass Spectrometry/Optical **Emission Spectrometry (ICP-MS/OES).** ICP-MS data were obtained with an Agilent 7700x ICP-MS and analyzed using ICP-MS Mass Hunter version B01.03. The samples were diluted in the 2% HNO₃ matrix and analyzed with a ¹⁵⁹Tb internal standard against a 12-point standard curve over the range from 0.1 to 500 ppb. The correlation was >0.9997 for all analyses of interest. Data collection was performed in Spectrum Mode with five replicates per sample and 100 sweeps per replicate. Solutions for ICP-MS were prepared by digesting 2 mg of material in 1 mL of HNO₃ (trace metal grade) solution in a fume hood overnight at room temperature. The solution was diluted with ultrafiltered deionized water for ICP-MS analysis. Reported errors are the standard deviation of measurements on three batches of each material.

An Agilent 700 series spectrometer was used for ICP-OES. The sample preparation was undertaken according to reported procedures 36 to improve the accuracy of sulfur determination. Solutions for ICP-OES were prepared by digesting 2 mg of materials in 0.5 mL of HNO₃ and 0.5 mL of H₂O₂ (trace metal grade) solutions in tightsealed high-density polyethylene centrifuge tubes overnight and then diluted with ultrafiltered deionized water. Reported errors are the standard deviation of measurements on three batches of each material.

X-ray Fluorescence (XRF) Measurements. XRF measurements were performed on pressed pellets with a Rigaku NEX DE VS spectrometer under a He atmosphere

X-ray Photoelectron Spectroscopy (XPS). XPS data were collected with an AXIS Nova spectrometer (Kratos Analytical) equipped with a monochromatic Al K_{\alpha} X-ray source. The Al anode was powered at 10 mA and 15 kV. The instrument work function was calibrated to give a Au $4f_{7/2}$ metallic gold binding energy of 83.95 eV. The instrument base pressure was ca. 5×10^{-9} Torr. The analysis area size was $0.3 \times 0.7 \text{ mm}^2$. For calibration purposes, the binding energies were referenced to the C 1s peak at 284.8 eV. Survey spectra were collected with a step size of 1 and 160 eV pass energy. UPS spectra were collected with an AXIS Nova spectrometer using a UV-radiation source. The high-resolution spectra were collected with a pass energy

of 20 and a 0.1 eV step size. Pressed pellets were affixed to conductive carbon tape under N_2 before loading into the spectrometer.

X-ray Absorption Spectroscopy (XAS). Powder samples of LiNiTTFtt and LiTHF-NiTTFtt were prepared by grinding finely with polypropylene as a binder. A Teflon washer (5.3 mm internal diameter) was sealed on one side with Kapton tape, and the ground powder was then transferred to the inside of this ring before compacting with a Teflon rod and sealing the remaining face with Kapton tape. XANES were employed to probe the local environment around Ni. Data were acquired at the Advanced Photon Source at Argonne National Laboratory with a bending magnet source with ring energy at 7.00 GeV. Ni K-edge (8333 eV) data were acquired at the MRCAT 10-BM beam line in transmission. The incident, transmitted, and reference X-ray intensities were monitored using gas ionization chambers. A metallic nickel foil standard was used as a reference for energy calibration and was measured simultaneously with experimental samples. X-ray absorption spectra were collected at room temperature. Data collected were processed using the Demeter software suite³⁷ by extracting the EXAFS oscillations $\chi(k)$ as a function of photoelectron wavenumber k. The theoretical paths were generated using FEFF6,38 and the models were done in the conventional way using the fitting program Artemis.

Infrared (IR) Spectroscopy. IR data were recorded on a Bruker Tensor II FTIR spectrometer with an MCT detector operated at 77 K. Data were processed and background corrected with the OPUS software (version 7.5). An additional manual correction for scattering was also applied. Samples were prepared under N_2 by grinding solid samples with Nujol, placed between two KBr crystal plates, and measured in air under ambient conditions.

Raman Spectroscopy. Raman spectroscopic data were obtained with a Horiba LabRamHR Evolution confocal microscope. A Si (111) wafer was used for calibration. The samples of 7 mm round pressed pellets were excited using a 532 nm light source operating at 5% of its power and using a 100× long path objective and a 600 mm⁻¹ grating. For the air-sensitive samples of Li-NiTTFtt and LiTHF-NiTTFtt, the pellets were sealed with additional glass slides and double-layer imaging spacers (Grace Secure Seal, 20 mm DIA × 0.12 mm Depth).

Solid-State Cyclic Voltammetry (CV). Electrochemical experiments were performed using CV on a BASi Epsilon potentiostat/ galvanostat. Then, 4 mg of fine powdery samples was added into 0.05 mL of N-methylpyrrolidone solution of 10 mg/mL polyvinylidene fluoride. After the resulting mixture was violently shaken, a few drops were pipetted onto the bottom of a glassy carbon electrode. After the solvent was mostly dried under ambient conditions, the glassy carbon electrode was further dried in a vial under vacuum overnight. In addition to the glassy carbon working electrode, a Pt flake and a Ag wire were used as the counter and reference electrodes, respectively. The reference electrode potential was measured vs the FeCp₂⁺/FeCp₂ couple in a separate solution of the relevant electrolyte (with a blank glassy carbon working electrode instead) to correct for the liquid junction potential. The CV experiments were taken in 0.1 M LiPF₆/ MeCN at a 10 mV/s scan rate for LiTHF-NiTTFtt and at a 5 mV/s scan rate for Li-NiTTFtt. All operations were done in a N2-filled

Room-Temperature Electrical Conductivity and Seebeck Measurements. Electrical conductivity measurements of LiTHF-NiTTFtt and Li-NiTTFtt were primarily performed in a two-contact geometry at room temperature under N₂. Samples were prepared as pressed pellets clamped between two brass electrodes (4.8 mm diam.) in a plastic sleeve, allowing measurement of the sample thickness with calipers. Linear sweep voltammetry was conducted using a BASi Epsilon potentiostat/galvanostat, with the reference and counter electrode terminals connected to one electrode and the working electrode terminal to the other. The resulting data were fit to a straight line to obtain the sample resistance. Reported errors are the standard deviation of measurements on four batches of each material.

As LiTHF-NiTTFtt is poorly conductive (about $10^{-6}-10^{-5}$ S/cm), two-probe conductivity measurements are roughly as accurate as four-probe methods since the instrument resistance ($\sim 1~\Omega$) is significantly smaller than the sample pellet.³⁹ Therefore, the electrical

conductivity of LiTHF-NiTTFtt is reported based on two-probe measurements. However, Li-NiTTFtt is fairly conductive, the conductivity of which would therefore be underestimated with two-probe measurements. Thus, in addition to the two-probe method, the conductivity of Li-NiTTFtt was also determined with a four-probe approach as discussed below.

The four-probe measurements of Li-NiTTFtt are based on a previously reported setup for NiTTFtt. 22,40 Gold electrical contacts (75 nm thick) for electronic conductivity (σ) and Seebeck coefficient (α) measurements were deposited onto 8 mm pressed pellets via thermal evaporation through homemade shadow masks. The electronic conductivity was measured in the in-plane direction by using a four-probe geometry with a 0.2 mm spacing between electrodes and electrode lengths of 1 mm. The Seebeck coefficient was measured with two 1 mm² gold pads, which are either 3 or 1 mm apart. A detailed schematic is shown in the previous report. Four probe conductivity measurements were performed using a customdesigned probe station in an argon glovebox. Voltage and current measurements were performed using a Keithley 2400 source meter and a Keithley 6221 precision current source. A constant current was applied to the outer contacts, and the resulting steady-state voltage response was recorded from the two inner contacts. The resistance (R, ohm) of the sample was extracted from the slope of the IV sweep by using Ohm's law (R = V/I). The conductivity σ $(1/\rho, \rho)$ is resistivity) was then calculated via the following equation:

$$\rho = \frac{V}{I} \frac{\pi t}{\left(\frac{\sinh\left(\frac{t}{s}\right)}{\sinh\left(\frac{t}{2s}\right)}\right)}$$

where t is the thickness of the sample and s is the separation distance between neighboring probes.

This formula has been previously applied for a thick Si wafer,⁴¹ which is similar to the round pressed pellet. The Seebeck coefficient measurements were performed on the same probe station. Two Peltier elements were placed 5 mm apart to provide the temperature difference ($\Delta T = T_H - T_C$). Two thermocouples were used to collect the hot and cold side temperatures, and two probes were used to measure the corresponding voltage value. A minimal amount of thermally conductive silicone paste was applied to the tips of the thermocouple to ensure good thermal contact between the thermocouple and the gold pads. A delay of 200 s was used for voltage measurements to ensure that a steady-state temperature gradient and voltage were reached. The measurements were taken within an approximate ΔT of ± 3 K around 300 K so that the Seebeck coefficient did not change significantly over $T \pm \Delta T$. A series of measurements on Ni foil (0.03 mm, >99.9%) were performed at 25 °C to determine the systematic error. The measured Seebeck coefficient of Ni is $-20.3 \pm 1.3 \,\mu\text{V/K}$, which matched well with reported values in the literature $(-19 \,\mu\text{V/K} \text{ at } 25\,^{\circ}\text{C}).^{42,43}$ While the Seebeck measurements were identical, the electrical conductivity of LiTHF-NiTTFtt was measured by using a two-probe method due to high resistivity.

Variable-Temperature Electrical Resistance. The as-synthesized powders of Li-NiTTFtt and LiTHF-NiTTFtt were pressed into 6 mm \times 6 mm squared pellets and cut into 2 mm \times 6 mm slides. The pellet slides were then mounted into the ceramic dual inline package (KYOCERA C-dip 16 pins), and two ends of pellets were connected with gold nodes by conductive silver paste. The variable temperature I-V measurements (two-probe) were carried out in a CRYOSTA-TION S50 system (Montana Instruments). For Li-NiTTFtt, the system was first cooled to 40 K and then slowly warmed up to target temperatures at a 10 K step to 200 K and then at a 20 K step until the sample thermally equilibrated at room temperature (295 K). At each temperature, the system was under vacuum and allowed to stabilize for 10 min before I-V profiles were collected from -100 to 100 mV. Ohmic I-V profiles were observed for all temperatures from 40 to 295 K, and a linear fit of the I-V curve was used to get the conductance (G) of the sample. Since the resistance of the LiTHF-NiTTFtt sample became large and out of the instrument's

measurement range, the conductance was recorded starting from 180 to 295 K with a 15 K step.

UV-vis-NIR diffuse reflectance spectroscopy data were collected using a Varian Cary 5000 spectrophotometer with powder samples loaded in a Praying Mantis air-free diffuse reflectance cell with KCl powder as the nonadsorbing matrix. The Kubelka-Munk conversion of the raw diffuse reflectance spectrum was obtained by applying the formula $F(R) = (1 - R)^2 / 2R$.

TGA was performed using a TA Instruments Discovery analyzer. Approximately 2 mg of sample was loaded into a pretared Pt pan and measured under N₂ or air. Samples were measured from 35 to 700 °C using a linear temperature ramp of 10 °C min⁻¹. During loading samples into the pan, samples had to be exposed to the air for about 1 min.

DSC for Li-NiTTFtt and NiTTFtt was performed using a TA Instruments Discovery analyzer. Approximately 7 mg of sample was sealed into a Tzero pan with a hermetic lid. The air-sensitive Li-NiTTFtt sample was sealed in a glovebox (the TA press was pumped into a glovebox). Under N2, the samples were measured in the temperature range of 20-150 °C using a linear temperature ramp of 10 °C min⁻¹ over two cycles.

Photothermal Conversion Measurements. An 8 mm round pellet of NiTTFtt (thickness 272 μ m) was placed in a white thermally insulated foam holder. The laser source is composed of a laser diode emitting at 808 nm (Thorlabs, L808P500MM) placed in a laser diode mount (Thorlabs, TCLDM9), which is controlled by a driver (TED 200C) and temperature controller (LDC 205C). An IR camera (FLIR, E30bx) was used as a temperature monitor. For Li-NiTTFtt, the setup is similar with minor adjustments: (1) a 7 mm round pellet was used; (2) the measurements were done in a N₂-filled glovebox instead of in-air; (3) while the IR camera was pumped into the glovebox, the laser source was still placed outside with the light coming through a quartz window and focused on the pellet by an adjusting mirror. The laser power for both cases was calibrated with a power sensor (Thorlabs, S310C).

NIR-Seebeck Voltage Measurements. For PTE experiments on Li-NiTTFtt, we used a similar setup in the glovebox but measured the Seebeck voltage with two probes connected to a multimeter (Agilent 34410A, associated with software, Keysight Benchvue). The probes were contacted with gold pads (on a homemade gold-deposited glass slide), which were connected to the pellet edges along a diametrical dimension using In wires and Ag paste. To avoid light shielding from the Ag paste, the face of the pellet that did not contain Ag paste was exposed to the light.

For NiTTFtt, since we found that the Ag paste was degraded in air after heating, some gold pads were deposited on the pellet's edge and used for direct connection with the probes. In order to create good electrical contacts between the gold pads and the probes, the soft foam substrate was replaced with thermally/electrically insulating Kapton tape.

ASSOCIATED CONTENT

Supporting Information

The Supporting Information is available free of charge at https://pubs.acs.org/doi/10.1021/jacs.2c07864.

> Additional experimental and calculation details, materials, and methods, including photographs of experimental setups (PDF)

AUTHOR INFORMATION

Corresponding Author

John S. Anderson - Department of Chemistry, University of Chicago, Chicago, Illinois 60637, United States; orcid.org/0000-0002-0730-3018; Email: jsanderson@ uchicago.edu

Authors

Jiaze Xie - Department of Chemistry, University of Chicago, Chicago, Illinois 60637, United States; o orcid.org/0000-0003-1813-9521

Jia-Ahn Pan – Department of Chemistry, University of Chicago, Chicago, Illinois 60637, United States; orcid.org/0000-0001-6153-8611

Baorui Cheng - Department of Chemistry, University of Chicago, Chicago, Illinois 60637, United States; Pritzker School of Molecular Engineering, University of Chicago, Chicago, Illinois 60637, United States

Tengzhou Ma - Pritzker School of Molecular Engineering, University of Chicago, Chicago, Illinois 60637, United States; o orcid.org/0000-0002-9116-5518

Alexander S. Filatov – Department of Chemistry, University of Chicago, Chicago, Illinois 60637, United States; orcid.org/0000-0002-8378-1994

Shrayesh N. Patel – Pritzker School of Molecular Engineering, University of Chicago, Chicago, Illinois 60637, United States; orcid.org/0000-0003-3657-827X

Jiwoong Park - Department of Chemistry, University of Chicago, Chicago, Illinois 60637, United States; Pritzker School of Molecular Engineering, University of Chicago, Chicago, Illinois 60637, United States

Dmitri V. Talapin – Department of Chemistry, University of Chicago, Chicago, Illinois 60637, United States; Pritzker School of Molecular Engineering, University of Chicago, Chicago, Illinois 60637, United States; o orcid.org/0000-0002-6414-8587

Complete contact information is available at: https://pubs.acs.org/10.1021/jacs.2c07864

Author Contributions

§J.X. and J.A.P. authors contributed equally.

Notes

The authors declare the following competing financial interest(s): We have a patent pending on this work. J.S.A. and J.X. have applied for a provisional patent on the materials described in this article. There are no further conflicts to declare.

ACKNOWLEDGMENTS

This work was supported by the Army Research Office under Grant W911NF-20-1-0091. J.S.A. acknowledges support from the U.S. Department of Energy (DOE), Office of Science, Office of Basic Energy Sciences, under Award DE-SC0019215, and from the National Science Foundation through grant DMR-2002367. D.V.T. and J.A.P. acknowledge support by the National Science Foundation under award CHE-1905290. The authors thank Daniel Laorenza and Prof. Danna Freedman for assistance with diffuse reflectance spectroscopy and Xiaomin Jiang, Yingjie Fan, Taokun Luo, and Prof. Wenbin Lin for assistance with ICP-MS measurements. The authors thank Maia Czaikowski for assistance with Raman spectroscopy and Garrett Grocke for the help of gold deposition and four-probe conductivity and Seebeck measurements. This research used resources of the Advanced Photon Source (APS) and the Center for Nanoscale Materials, U.S. Department of Energy Office of Science User Facilities operated for the DOE Office of Science by Argonne National Laboratory under Contract No. DE-AC02-06CH11357. We thank McKenna Goetz and beamline staffs for assistance with XAS measurements at

beamline APS 10-BM-A, B. Parts of this work were carried out at the Soft Matter Characterization Facility of the University of Chicago. This work made use of the shared facilities at the University of Chicago Materials Research Science and Engineering Center, supported by National Science Foundation under award number DMR-2011854.

REFERENCES

- (1) (a) Mills, D. Advances in Solar Thermal Electricity Technology. Sol. Energy 2004, 76, 19-31. (b) Roeb, M.; Müller-Steinhagen, H. Concentrating on Solar Electricity and Fuels. Science 2010, 329, 773-
- (2) (a) Ueno, K.; Oshikiri, T.; Sun, Q.; Shi, X.; Misawa, H. Solid-State Plasmonic Solar Cells. Chem. Rev. 2018, 118, 2955-2993. (b) Cheng, Y.-J.; Yang, S.-H.; Hsu, C.-S. Synthesis of Conjugated Polymers for Organic Solar Cell Applications. Chem. Rev. 2009, 109, 5868-5923. (c) Jena, A. K.; Kulkarni, A.; Miyasaka, T. Halide Perovskite Photovoltaics: Background, Status, and Future Prospects. Chem. Rev. 2019, 119, 3036-3103.
- (3) Kim, J. Y.; Lee, J.-W.; Jung, H. S.; Shin, H.; Park, N.-G. High-Efficiency Perovskite Solar Cells. Chem. Rev. 2020, 120, 7867-7918.
- (4) Polman, A.; Atwater, H. A. Photonic Design Principles for Ultrahigh-Efficiency Photovoltaics. Nat. Mater. 2012, 11, 174-177.
- (5) (a) Zhao, X.; Yao, C.; Liu, T.; Hamill, J. C.; Ngongang Ndjawa, G. O.; Cheng, G.; Yao, N.; Meng, H.; Loo, Y. Extending the Photovoltaic Response of Perovskite Solar Cells into the Near-Infrared with a Narrow-Bandgap Organic Semiconductor. Adv. Mater. 2019, 31, No. 1904494. (b) Bai, Y.; Lang, K.; Zhao, C.; Guo, Q.; Zeng, R.; Wang, J.; Hayat, T.; Alsaedi, A.; Tan, Z. Strategies Toward Extending the Near-Infrared Photovoltaic Response of Perovskite Solar Cells. Sol. RRL 2020, 4, No. 1900280.
- (6) (a) Kraemer, D.; Poudel, B.; Feng, H.-P.; Caylor, J. C.; Yu, B.; Yan, X.; Ma, Y.; Wang, X.; Wang, D.; Muto, A.; McEnaney, K.; Chiesa, M.; Ren, Z.; Chen, G. High-Performance Flat-Panel Solar Thermoelectric Generators with High Thermal Concentration. Nat. Mater. 2011, 10, 532-538. (b) Park, T.; Na, J.; Kim, B.; Kim, Y.; Shin, H.; Kim, E. Photothermally Activated Pyroelectric Polymer Films for Harvesting of Solar Heat with a Hybrid Energy Cell Structure. ACS Nano 2015, 9, 11830-11839. (c) Limpert, S.; Burke, A.; Chen, I.-J.; Anttu, N.; Lehmann, S.; Fahlvik, S.; Bremner, S.; Conibeer, G.; Thelander, C.; Pistol, M.-E.; Linke, H. Bipolar Photothermoelectric Effect Across Energy Filters in Single Nanowires. Nano Lett. 2017, 17, 4055-4060.
- (7) (a) Liu, H.; Liu, Y.; Dong, S.; Xu, H.; Wu, Y.; Hao, L.; Cao, B.; Li, M.; Wang, Z.; Han, Z.; Yan, K. Photothermoelectric SnTe Photodetector with Broad Spectral Response and High On/Off Ratio. ACS Appl. Mater. Interfaces 2020, 12, 49830-49839. (b) Wang, F.; Lv, Y.; Xu, Y.; Cao, L.; Chen, L.; Zhang, C.; Yao, S.; Xu, J.; Zhou, J.; Chen, Y. Enhanced Photothermoelectric Detection in Co:BiCuSeO Crystals with Tunable Seebeck Effect. Opt. Express 2022, 30, 8356.
- (8) Koyama, S.; Inaba, Y.; Kasano, M.; Murata, T. A Day and Night Vision MOS Imager With Robust Photonic-Crystal-Based RGB-and-IR. IEEE Trans. Electron Devices 2008, 55, 754-759.
- (9) Lu, X.; Sun, L.; Jiang, P.; Bao, X. Progress of Photodetectors Based on the Photothermoelectric Effect. Adv. Mater. 2019, 31, No. 1902044.
- (10) (a) Antidormi, A.; Cummings, A. W. Optimizing the Photothermoelectric Effect in Graphene. Phys. Rev. Appl. 2021, 15, No. 054049. (b) Yamashita, H.; Tsunoda, K.; Nishino, H.; Sato, S. Signal-to-Noise Characteristics of Graphene Photodetectors Based on Photothermoelectric Effect. J. Appl. Phys. 2021, 129, 173101. ((c)) Viti, L.; Cadore, A. R.; Yang, X.; Vorobiev, A.; Muench, J. E.; Watanabe, K.; Taniguchi, T.; Stake, J.; Ferrari, A. C.; Vitiello, M. S.Thermoelectric Graphene Photodetectors with Sub-Nanosecond Response Times at Terahertz Frequencies. In Frontiers in Optics and Photonics; De Gruyter, 2021; Vol. 10, pp. 89-98
- (11) Buscema, M.; Barkelid, M.; Zwiller, V.; van der Zant, H. S. J.; Steele, G. A.; Castellanos-Gomez, A. Large and Tunable Photo-

- thermoelectric Effect in Single-Layer MoS₂. Nano Lett. 2013, 13, 358 - 363.
- (12) Kim, B.; Shin, H.; Park, T.; Lim, H.; Kim, E. NIR-Sensitive Poly(3,4-Ethylenedioxyselenophene) Derivatives for Transparent Photo-Thermo-Electric Converters. Adv. Mater. 2013, 25, 5483-
- (13) Huang, D.; Zou, Y.; Jiao, F.; Zhang, F.; Zang, Y.; Di, C.; Xu, W.; Zhu, D. Interface-Located Photothermoelectric Effect of Organic Thermoelectric Materials in Enabling NIR Detection. ACS Appl. Mater. Interfaces 2015, 7, 8968-8973.
- (14) (a) Wang, Y.; Zhu, W.; Du, W.; Liu, X.; Zhang, X.; Dong, H.; Hu, W. Cocrystals Strategy towards Materials for Near-Infrared Photothermal Conversion and Imaging. Angew. Chem. Int. Ed. 2018, 57, 3963-3967. (b) Su, J.; Xu, N.; Murase, R.; Yang, Z.; D'Alessandro, D. M.; Zuo, J.; Zhu, J. Persistent Radical Tetrathiafulvalene-Based 2D Metal-Organic Frameworks and Their Application in Efficient Photothermal Conversion. Angew. Chem. Int. Ed. 2021, 60, 4789-4795. (c) Yan, T.; Li, Y.; Su, J.; Wang, H.; Zuo, J. Charge Transfer Metal-Organic Framework Containing Redox-Active TTF/NDI Units for Highly Efficient Near-Infrared Photothermal Conversion. Chem. -A Eur. J. 2021, 27, 11050-11055. (d) Yan, T.; Li, Y.-Y.; Gu, Q.-Y.; Li, J.; Su, J.; Wang, H.-Y.; Zuo, J.-L. A Tetrathiafulvalene/Naphthalene Diimide-Containing Metal-Organic Framework with Fsc Topology for Highly Efficient Near-Infrared Photothermal Conversion. Inorg. Chem. 2022, 61, 3078-3085.
- (15) (a) Sun, L.; Campbell, M. G.; Dinca, M. Electrically Conductive Porous Metal-Organic Frameworks. Angew. Chem. Int. Ed. 2016, 55, 3566-3579. (b) Xie, L. S.; Skorupskii, G.; Dincă, M. Electrically Conductive Metal-Organic Frameworks. Chem. Rev. 2020, 120, 8536-8580.
- (16) Huang, X.; Zhang, S.; Liu, L.; Yu, L.; Chen, G.; Xu, W.; Zhu, D. Superconductivity in a Copper(II)-Based Coordination Polymer with Perfect Kagome Structure. Angew. Chem. Int. Ed. 2018, 57, 146-150. (17) Liu, J.; Song, X.; Zhang, T.; Liu, S.; Wen, H.; Chen, L. 2D Conductive Metal-Organic Frameworks: An Emerging Platform for Electrochemical Energy Storage. Angew. Chem. Int. Ed. 2021, 60, 5612-5624.
- (18) (a) Sun, Y.; Sheng, P.; Di, C.; Jiao, F.; Xu, W.; Qiu, D.; Zhu, D. Organic Thermoelectric Materials and Devices Based on P- and n-Type Poly(Metal 1,1,2,2-Ethenetetrathiolate)S. Adv. Mater. 2012, 24, 932-937. (b) Jiao, F.; Di, C.; Sun, Y.; Sheng, P.; Xu, W.; Zhu, D. Inkjet-Printed Flexible Organic Thin-Film Thermoelectric Devices Based on p- and n-Type Poly(Metal 1,1,2,2-Ethenetetrathiolate)s/ Polymer Composites through Ball-Milling. Philos. Trans. R. Soc. A Math. Phys. Eng. Sci. 2013, 2014, No. 20130008. (c) Sun, Y.; Qiu, L.; Tang, L.; Geng, H.; Wang, H.; Zhang, F.; Huang, D.; Xu, W.; Yue, P.; Guan, Y.; Jiao, F.; Sun, Y.; Tang, D.; Di, C.; Yi, Y.; Zhu, D. Flexible N-Type High-Performance Thermoelectric Thin Films of Poly(Nickel-Ethylenetetrathiolate) Prepared by an Electrochemical Method. Adv. Mater. 2016, 28, 3351-3358. (d) Sun, L.; Liao, B.; Sheberla, D.; Kraemer, D.; Zhou, J.; Stach, E. A.; Zakharov, D.; Stavila, V.; Talin, A. A.; Ge, Y.; Allendorf, M. D.; Chen, G.; Léonard, F.; Dincă, M. A Microporous and Naturally Nanostructured Thermoelectric Metal-Organic Framework with Ultralow Thermal Conductivity. Joule 2017, 1, 168-177.
- (19) (a) Noro, S.; Chang, H.-C.; Takenobu, T.; Murayama, Y.; Kanbara, T.; Aoyama, T.; Sassa, T.; Wada, T.; Tanaka, D.; Kitagawa, S.; Iwasa, Y.; Akutagawa, T.; Nakamura, T. Metal-Organic Thin-Film Transistor (MOTFT) Based on a Bis(o -Diiminobenzosemiquinonate) Nickel(II) Complex. J. Am. Chem. Soc. 2005, 127, 10012-10013. (b) Miner, E. M.; Fukushima, T.; Sheberla, D.; Sun, L.; Surendranath, Y.; Dincă, M. Electrochemical Oxygen Reduction Catalysed by Ni₃(Hexaiminotriphenylene)₂. Nat. Commun. 2016, 7, 10942. (c) Huang, X.; Yao, H.; Cui, Y.; Hao, W.; Zhu, J.; Xu, W.; Zhu, D. Conductive Copper Benzenehexathiol Coordination Polymer as a Hydrogen Evolution Catalyst. ACS Appl. Mater. Interfaces 2017, 9, 40752-40759. (d) DeGayner, J. A.; Jeon, I.-R.; Sun, L.; Dincă, M.; Harris, T. D. 2D Conductive Iron-Quinoid Magnets Ordering up to T_c = 105 K via Heterogenous Redox Chemistry. J. Am. Chem. Soc.

- 2017, 139, 4175–4184. (e) Hoppe, B.; Hindricks, K. D. J.; Warwas, D. P.; Schulze, H. A.; Mohmeyer, A.; Pinkvos, T. J.; Zailskas, S.; Krey, M. R.; Belke, C.; König, S.; Fröba, M.; Haug, R. J.; Behrens, P. Graphene-like Metal—Organic Frameworks: Morphology Control, Optimization of Thin Film Electrical Conductivity and Fast Sensing Applications. *CrystEngComm* 2018, 20, 6458–6471.
- (20) Kusamoto, T.; Nishihara, H. Zero-, One- and Two-Dimensional Bis(Dithiolato)Metal Complexes with Unique Physical and Chemical Properties. *Coord. Chem. Rev.* **2019**, *380*, 419–439.
- (21) Camerel, F.; Fourmigué, M. (Photo)Thermal Stimulation of Functional Dithiolene Complexes in Soft Matter. *Eur. J. Inorg. Chem.* **2020**, 2020, 508–522.
- (22) Xie, J.; Ewing, S.; Boyn, J. N.; Filatov, A. S.; Cheng, B.; Ma, T.; Grocke, G.; Zhao, N.; Itani, R.; Sun, X.; Cho, H.; Chen, Z.; Chapman, K. W.; Patel, S. N.; Talapin, D. V.; Park, J.; Mazziotti, D. A.; Aderson, J. S. *Nature*, accepted, DOI: 10.1038/s41586-022-05261-
- (23) Xie, J.; Boyn, J. N.; Filatov, A. S.; McNeece, A. J.; Mazziotti, D. A.; Anderson, J. S. Redox, Transmetalation, and Stacking Properties of Tetrathiafulvalene-2,3,6,7-Tetrathiolate Bridged Tin, Nickel, and Palladium Compounds. *Chem. Sci.* **2020**, *11*, 1066–1078.
- (24) Scott, R. A. Comparative X-ray absorption spectroscopic structural characterization of nickel metalloenzyme active sites. *Phys. B* **1989**, *158*, 84–86.
- (25) de Caro, D.; Fraxedas, J.; Faulmann, C.; Malfant, I.; Milon, J.; Lamère, J.-F.; Collière, V.; Valade, L. Metallic Thin Films of TTF[Ni(Dmit)₂]₂ by Electrodeposition on (001)-Oriented Silicon Substrates. *Adv. Mater.* **2004**, *16*, 835–838.
- (26) (a) Rivera, N. M.; Engler, E. M.; Schumaker, R. R. Synthesis and Properties of Tetrathiafulvalene-Metal Bisdithiolene Macromolecules. J. Chem. Soc., Chem. Commun. 1979, 4, 184-185. (b) Poleschner, H.; John, W.; Hoppe, F.; Fanghänel, E.; Roth, S. Tetrathiafulvalene. XIX. Synthese Und Eigenschaften Elektronenleitender Poly-Dithiolenkomplexe Mit Ethylentetrathiolat Und Tetrathiafulvalentetrathiolat Als Brückenliganden. J. Prakt. Chem. 1983, 325, 957-975. (c) Vogt, T.; Faulmann, C.; Soules, R.; Lecante, P.; Mosset, A.; Castan, P.; Cassoux, P.; Galy, J. A LAXS (Large Angle X-Ray Scattering) and EXAFS (Extended X-Ray Absorption Fine Structure) Investigation of Conductive Amorphous Nickel Tetrathiolato Polymers. J. Am. Chem. Soc. 1988, 110, 1833-1840. (d) Yoshioka, N.; Nishide, H.; Inagaki, K.; Inagaki, K.; Tsuchida, E. Electrical Conductive and Magnetic Properties of Conjugated Tetrathiolate Nickel Polymers. Polym. Bull. 1990, 23, 631-636. (e) Dahm, S.; Strunz, W.; Keller, H. J.; Schweitzer, D. Preparation and Physical Properties of Highly Conducting Metal (M = Ni, Co, Cu) Coordination Polymers. Synth. Met. 1993, 55, 884-889.
- (27) Halim, J.; Moon, E. J.; Eklund, P.; Rosen, J.; Barsoum, M. W.; Ouisse, T. Variable Range Hopping and Thermally Activated Transport in Molybdenum-Based MXenes. *Phys. Rev. B* **2018**, 98, No. 104202.
- (28) Kobayashi, A.; Fujiwara, E.; Kobayashi, H. Single-Component Molecular Metals with Extended-TTF Dithiolate Ligands. *Chem. Rev.* **2004**, *104*, 5243–5264.
- (29) Kobayashi, Y.; Terauchi, T.; Sumi, S.; Matsushita, Y. Carrier Generation and Electronic Properties of a Single-Component Pure Organic Metal. *Nat. Mater.* **2017**, *16*, 109–114.
- (30) Paściak, A.; Pilch-Wróbel, A.; Marciniak, Ł.; Schuck, P. J.; Bednarkiewicz, A. Standardization of Methodology of Light-to-Heat Conversion Efficiency Determination for Colloidal Nanoheaters. *ACS Appl. Mater. Interfaces* **2021**, *13*, 44556–44567.
- (31) Zhao, Y.; He, Z.; Zhang, Q.; Wang, J.; Jia, W.; Jin, L.; Zhao, L.; Lu, Y. 880 nm NIR-Triggered Organic Small Molecular-Based Nanoparticles for Photothermal Therapy of Tumor. *Nanomaterials* **2021**, *11*, 773.
- (32) Yang, H.; Fu, B.; Li, D.; Tian, Y.; Chen, Y.; Mattila, M.; Yong, Z.; Li, R.; Hassanien, A.; Yang, C.; Tittonen, I.; Ren, Z.; Bai, J.; Li, Q.; Kauppinen, E. I.; Lipsanen, H.; Sun, Z. Broadband Laser Polarization Control with Aligned Carbon Nanotubes. *Nanoscale* **2015**, *7*, 11199–11205.

- (33) Bubnova, O.; Khan, Z. U.; Malti, A.; Braun, S.; Fahlman, M.; Berggren, M.; Crispin, X. Optimization of the Thermoelectric Figure of Merit in the Conducting Polymer Poly(3,4-Ethylenedioxythiophene). *Nat. Mater.* **2011**, *10*, 429–433.
- (34) (a) Cao, R.; Sun, D.; Wang, L.; Yan, Z.; Liu, W.; Wang, X.; Zhang, X. Enhancing Solar—Thermal—Electric Energy Conversion Based on m-PEGMA/GO Synergistic Phase Change Aerogels. *J. Mater. Chem. A* **2020**, *8*, 13207—13217. (b) Zhang, Y.; Wu, K.; Fu, Q. A Structured Phase Change Material with Controllable Thermoconductive Highways Enables Unparalleled Electricity via Solar-Thermal-Electric Conversion. *Adv. Funct. Mater.* **2022**, *32*, No. 2109255.
- (35) Boudier, A.; Breuil, P.-A. R.; Magna, L.; Olivier-Bourbigou, H.; Braunstein, P. Nickel(II) Complexes with Imino-Imidazole Chelating Ligands Bearing Pendant Donor Groups (SR, OR, NR₂, PR₂) as Precatalysts in Ethylene Oligomerization. *J. Organomet. Chem.* **2012**, 718, 31–37.
- (36) Morrison, C.; Sun, H.; Yao, Y.; Loomis, R. A.; Buhro, W. E. Methods for the ICP-OES Analysis of Semiconductor Materials. *Chem. Mater.* **2020**, 32, 1760–1768.
- (37) Ravel, B.; Newville, M. ATHENA, ARTEMIS, HEPHAES-TUS: Data Analysis for X-Ray Absorption Spectroscopy Using IFEFFIT. J. Synchrotron Radiat. 2005, 12, 537–541.
- (38) Rehr, J. J.; Albers, R. C. Theoretical Approaches to X-Ray Absorption Fine Structure. *Rev. Mod. Phys.* **2000**, 72, 621–654.
- (39) Sun, L.; Park, S. S.; Sheberla, D.; Dincă, M. Measuring and Reporting Electrical Conductivity in Metal-Organic Frameworks: Cd₂(TTFTB) as a Case Study. *J. Am. Chem. Soc.* **2016**, *138*, 14772–14782
- (40) Ma, T.; Dong, B. X.; Grocke, G. L.; Strzalka, J.; Patel, S. N. Leveraging Sequential Doping of Semiconducting Polymers to Enable Functionally Graded Materials for Organic Thermoelectrics. *Macromolecules* **2020**, *53*, 2882–2892.
- (41) Schroder, D.Semiconductor material and device characterization, 3rd ed.; IEEE Press; Wiley: Piscataway, NJ; Hoboken, NJ, 2006.
- (42) Schmidt, V.; Mensch, P. F. J.; Karg, S. F.; Gotsmann, B.; Das Kanungo, P.; Schmid, H.; Riel, H. Using the Seebeck Coefficient to Determine Charge Carrier Concentration, Mobility, and Relaxation Time in InAs Nanowires. *Appl. Phys. Lett.* **2014**, *104*, No. 012113.
- (43) Beretta, D.; Bruno, P.; Lanzani, G.; Caironi, M. Reliable Measurement of the Seebeck Coefficient of Organic and Inorganic Materials between 260 K and 460 K. Rev. Sci. Instrum. 2015, 86, No. 075104.